17

Towards noninvasive glucose sensing using polarization analysis of multiply scattered light

Michael F. G. Wood, Nirmalya Ghosh, Xinxin Guo and I. Alex Vitkin

Division of Biophysics and Bioimaging, Ontario Cancer Institute and Department of Medical Biophysics, University of Toronto Toronto, Ontario, Canada

17.1 Introduction 470
17.2 Polarimetry in turbid media: experimental platform for sensitive polarization measurements in the presence of large depolarized noise 472
17.3 Polarimetry in turbid media: accurate forward modeling using the Monte Carlo approach 478
17.4 Tackling the inverse problem: polar decomposition of the lumped Mueller matrix to extract individual polarization contributions 482
17.5 Monte Carlo modeling results for measurement geometry, optical pathlength, detection depth, and sampling volume quantification 489
17.6 Combining intensity and polarization information via spectroscopic turbid polarimetry with chemometric analysis 494
17.7 Concluding remarks on the prospect of glucose detection in optically thick scattering tissues with polarized light 499
Acknowledgements 500
References 501

This chapter introduces the concept of polarized light measurements in biological tissues. Polarimetry has a long and successful history in various forms of clear media. However, as tissue is a complex random medium that causes multiple scattering of light and thus extensive depolarization, a polarimetric approach for tissue characterization may at first seem surprising. Nevertheless, we and others have shown that multiple scattering does not fully depolarize the light, and reliable measurements and analyzes of surviving polarized light fractions can be made in some situations. As polarized light interacts with optically-active molecules such as glucose in characteristic ways, the possibility arises of measuring a glucose polarization signal in light multiply scattered by tissue. We therefore describe the variety of experimental and theoretical tools, illustrated with selected results, aimed at evaluating the prospect of

noninvasive glucose detection via turbid polarimetry.

17.1 Introduction

Non-invasive glucose monitoring in diabetic patients remains one of the most important unsolved problems in modern medicine. The problem is indeed getting more acute, as the incidence of type II diabetes continues to grow at an alarming rate. Tight regulation of glucose levels is needed to avoid long-term health complications, thus the crucial need exists to measure these levels in order to regulate insulin and caloric intakes, exercise regiments, and so forth. Unfortunately, the most reliable current method necessitates the drawing of blood, usually by a finger prick. Because of the inconvenience, many diabetics do not comply with the required minimum of 5 times a day determination regimen, and instead rely on their symptoms and experience to guide caloric intake and insulin administration. Because of the tremendous clinical importance of this problem and its huge commercial potential, a significant research effort has been undertaken, and is ongoing, in finding a noninvasive replacement for the finger-prick way for measuring blood glucose levels. Research and commercial activities have been intense, and have included fully non-invasive, as well as minimally invasive approaches (*e.g.*, glucose-drawing patch, glucose-sensitive fluorescent tattoos, implantable sensors). A subset of actively investigated techniques involves optical methods, as described in detail in the different chapters of the present volume.

A common difficulty with the various proposed noninvasive techniques is the indirect, and often weak, relationship between the change in the measured signal and the corresponding change in the absolute glucose levels. This results in a lack of sensitivity (small signal changes) and, perhaps more importantly, a lack of specificity, in that many other glucose-unrelated factors can cause similar small signal changes. This is referred to as the calibration problem, and various approaches to its solution have been reviewed [1]. Optical polarimetry is particularly promising in this respect [2, 3], in that its measurable polarization parameters (*e.g.*, optical rotation) can be directly related to the absolute glucose levels. Specifically, glucose is an optically active (chiral) molecule that rotates the plane of linearly polarized light by an amount proportional to its concentration and the optical pathlength. This proportionality is described in Eq. (17.1), and has been verified numerous times in *clear* media; in fact, one of earliest application of polarimetry relied on this relationship to determine sugar concentration in industrial production processes [4]:

$$\alpha = R(\lambda, T) \cdot C \cdot \langle L \rangle \tag{17.1}$$

In Eq. (17.1) α is the measured optical rotation, R is the (known) rotatory power of the molecular species (*e.g.*, glucose) at a particular light wavelength λ and temperature T, C is the concentration (of glucose) to be determined, and $\langle L \rangle$ is the optical

pathlength. This simple linear relationship is exploited for the glucose monitoring problem in the only transparent tissue in the body, specifically the eye. Chapter 15 of this monograph describes the exciting research in developing a glucose sensor by polarimetric measurements through the aqueous humor of the eye that can be related to blood glucose levels, and outlines the remaining outstanding challenges of this promising approach.

With the exception of transparent ocular tissues, however, the human body is highly absorbing and scattering in the UV-IR range, and the validity of Eq. (17.1) is questionable. Specifically, (i) light is highly depolarized upon tissue multiple scattering, so even initial detection of a polarization-preserved signal from which to attempt glucose concentration extraction is a formidable challenge; (ii) the optical pathlength $\langle L \rangle$ in turbid media is a difficult quantity to define, quantify, and measure, and really represents a statistical distribution metric of a variety of photon paths that depend in a complex way on tissue optical properties and measurement geometry, (iii) other optically active chiral species are present in tissue, thus contributing to the observed optical rotation and hiding/confounding the specific glucose contribution, (iv) several optical polarization effects occur in tissue simultaneously (*e.g.*, optical rotation, birefringence, absorption, depolarization), contributing to the resultant polarization signals in a complex interrelated way and hindering their unique interpretation.

Despite these difficulties, we and others have recently shown that even in the presence of severe depolarization, measurable polarization signals can be reliably obtained from highly scattering media such as biological tissue. We have demonstrated surviving linear and circular polarization fractions of light scattered from optically thick turbid media, and measured the resulting optical rotations of the linearly polarized light [5 - 10]. A comprehensive polarization-sensitive Monte Carlo model has complemented our experimental studies by helping with signal interpretation and analysis, validation of novel approaches, quantification of variables of interest, and guidance in experimental design optimization. Further, we have developed various experimental and analytical methods to maximize polarization sensitivity, quantify pathlength distributions of polarized and depolarized light in multiple scattering media, model the effect of several simultaneous optical effects that can mask the glucose polarization signature, and examine the utility of spectroscopic methods to account for the polarization effects of glucose-unrelated confounding species. In this chapter, we summarize this (and related) research on turbid polarimetry, and discuss the implication of this approach for the human glucose detection problem.

This chapter is organized as follows. In section 17.2, we describe the high-sensitivity polarization modulation / synchronous detection experimental system capable of measuring small polarization signals in the presence of large depolarized background of multiply scattered light. Both Stokes vectors and Mueller matrix approaches are discussed. This is followed by the description of the corresponding theoretical model in section 17.3, based on the forward Monte Carlo (MC) modeling, with the flexibility to incorporate all the simultaneous optical effects; selected validation studies of both the MC model and the experimental methodology are presented. Having established the ability to accurately measure and model turbid polarimetry signals, we now turn to the complicated inverse problem of separating out the con-

stituent contributions from simultaneous optical effects; thus, section 17.4 reviews the polar decomposition studies aimed at quantifying individual contributions from 'lumped' Mueller matrix experimental results. Section 17.5 deals with the quantification of the polarized pathlength / sampling volume effects in turbid media, and examines the effects of experimental geometry. In section 17.6, we discuss the initial results of spectral chemometric studies, aimed at combining turbid polarimetry data with diffuse reflectance data, in order to increase the glucose-related information content and to (spectrally) filter out the confounding effects of other tissue constituents. The chapter concludes with a discussion of the applicability of the turbid polarimetry approach to the noninvasive glucose detection problem.

17.2 Polarimetry in turbid media: experimental platform for sensitive polarization measurements in the presence of large depolarized noise

In order to perform accurate glucose concentration measurements in scattering media such as biological tissues, a highly sensitive polarimetry system is required. Multiple scattering leads to depolarization of light, creating a large depolarized source of noise that hinders the detection of the small remaining information-carrying polarization signal. One possible method to detect these small polarization signals is the use of polarization modulation with synchronous lock-in-amplifier detection. Many sensitive detection schemes are possible with this approach [5 - 12]. Some perform polarization modulation on the light that interrogates the tissue sample; others modulate the light that has interacted with the sample, placing the polarization modulator between the sample and the detector. The resultant signal, when analyzed in the context of Mueller matrix/Stokes vector formalism (see below), can yield sample-specific polarization properties that can then be linked to the quantities of interest (as, for example, linking glucose concentration to the measured optical rotation, provided that some form of Eq. (17.1) applies in turbid media). By way of illustration, we describe below a particular experimental embodiment of the polarization modulation/synchronous detection. This arrangement carries the advantage of being assumption-independent, in that no functional form of the sample polarization effects is assumed [5]. This turns out to be quite important in complex media such as tissues, since there are typically several polarization-altering effects occurring simultaneously. Thus, a unique and unambiguous tissue polarization description is difficult, so an approach that does not requite assumptions on how tissue alters polarized light, but rather determines it directly, is preferred.

The described methodology can yield both Stokes vector of the light exiting the sample and calculate its Mueller matrix. A Stokes vector **S** is comprised of four elements completely describing the polarization of a light beam, $\mathbf{S} = (IQUV)^T$. The first element I represent the overall intensity of the beam, the second element Q rep-

resents the amount linearly polarized light in the horizontal and vertical planes, the third element U represents the amount of linearly polarized light in the $\pm 45^\circ$ planes, and the final element V represents the amount of circularly polarized light. The interactions of polarized light with any optical element, including the tissue sample being examined, are applied to the polarization of a light beam through multiplication of the incident Stokes vector with a 4×4 Mueller matrix $\mathbf{M}$. Given an input Stokes vector $\mathbf{S}_i$ impinging on a polarization affecting element, the output Stokes vector $\mathbf{S}_o$ is given as $\mathbf{S}_o = \mathbf{M}\mathbf{S}_i$. Both the measured Stokes vector and calculated Mueller matrix can be used to quantify the polarizing properties of the sample, including optical rotation produced by optically active (chiral) molecules such as glucose.

A schematic of our current turbid polarimetry system is shown in Fig. 17.1 [5]. Unpolarized light is used to seed the system; the experimental results reported here are for a 632.8 nm HeNe laser excitation. Spectroscopic excitation (possibly white-light source with a monochromator) may be preferable in the future, as suggested by the chemometric analysis of spectral polarimetry data (section 17.6). The light first passes through a mechanical chopper operating at a frequency $f_c \sim 500$ Hz; this is used in conjunction with lock-in amplifier detection to accurately establish the overall signal intensity levels, as described below. The input optics (a linear polarizer with/without the quarter wave-plate) allow for complete control of the input light polarization that interrogates the sample. The light that has interacted with the sample is detected at a choosen direction as the detection optics can be rotated around the sample. The detection optics begin with a removable quarter wave plate oriented at -45° to the horizontal plane: when present, Stokes parameters Q and U (linear polarization descriptors) are measured, and the Stokes parameter V (circular polarization descriptor) when removed. Sample-scattered light then passes through a photoelastic modulator (PEM), which is a linearly birefringent resonant device operating at $f_p = 50$ kHz. Its fast axis at 0° and its retardation is modulated according to the sinusoidal function $\delta_{\mathrm{PEM}}(t) = \delta_0 \sin(\omega t)$, where $\omega_p = 2\pi f_p$ and δ_0 is the user-specified amplitude of PEM maximum retardation. The light finally passes through a linear analyzer orientated at 45°, converting the PEM-imparted polarization modulation to an intensity modulation suitable for photodetection. The detected signal is sent to a lock-in amplifier, with its reference input toggled between the chopper and PEM frequencies for synchronous detection of their respective signals.

The data analysis proceeds as follows. The Stokes vector that carries the sample-specific information, is given as (detection quarter wave-plate in place):

$$\begin{pmatrix} I_f \\ Q_f \\ U_f \\ V_f \end{pmatrix} = \frac{1}{2} \begin{pmatrix} 1\,0\,1\,0 \\ 0\,0\,0\,0 \\ 1\,0\,1\,0 \\ 0\,0\,0\,0 \end{pmatrix} \begin{pmatrix} 1\,0\,0 & 0 \\ 0\,1\,0 & 0 \\ 0\,0\,\cos\delta & \sin\delta \\ 0\,0\,-\sin\delta & \cos\delta \end{pmatrix} \begin{pmatrix} 1\,0 & 0\,0 \\ 0\,0 & 0\,1 \\ 0\,0 & 1\,0 \\ 0\,-1 & 0\,0 \end{pmatrix} \begin{pmatrix} I \\ Q \\ U \\ V \end{pmatrix} \tag{17.2}$$

and when the detection quarter wave-plate is removed as,

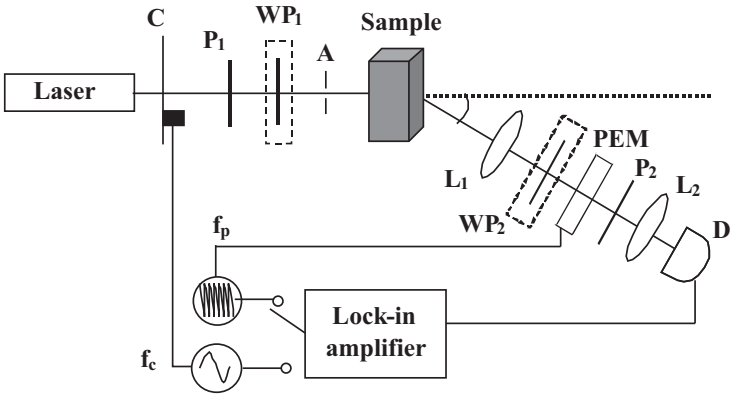

FIGURE 17.1: Schematic of the turbid polarimeter. C, mechanical chopper; P_1, P_2, polarizers; WP_1, WP_2, removable quarter wave plates; A, aperture; L_1, L_2 lenses; PEM, photoelastic modulator; D, photodetector; f_c, f_p modulation frequencies of mechanical chopper and PEM, respectively. The detection optics can be rotated by an angle θ around the sample (adapted from reference [5]).

$$\begin{pmatrix} I_{fr} \\ Q_{fr} \\ U_{fr} \\ V_{fr} \end{pmatrix} = \frac{1}{2} \begin{pmatrix} 1\,0\,1\,0 \\ 0\,0\,0\,0 \\ 1\,0\,1\,0 \\ 0\,0\,0\,0 \end{pmatrix} \begin{pmatrix} 1\,0\,0 & 0 \\ 0\,1\,0 & 0 \\ 0\,0\,\cos\delta & \sin\delta \\ 0\,0\,-\sin\delta & \cos\delta \end{pmatrix} \begin{pmatrix} I \\ Q \\ U \\ V \end{pmatrix} \tag{17.3}$$

The detected intensity signals are thus ($q = Q/I$, $u = U/I$, and $v = V/I$)

$$I_f(t) = \frac{I}{2}[1 - q\sin\delta + u\cos\delta]; \tag{17.4}$$

$$I_{fr} = \frac{I}{2}[1 - v\sin\delta + u\cos\delta], \tag{17.5}$$

where $\delta = \delta(t) = \delta_0 \sin\omega t$ is the time-varying PEM retardation of user-specified δ_0 magnitude. A time-varying circular function in the argument of another circular function, as is present in Equations (17.3) and (17.4), can be Fourier expanded in terms of Bessel functions [13] to yield signals at different harmonics of the fundamental modulation frequency. It can be advantageous in terms of SNR to choose the peak retardance of the PEM such that the zeroth order-Bessel function J_0 is zero [10]; with this selection of $\delta_0 = 2.405$ radians (resulting in $J_0(\delta_0) = 0$), Fourier-Bessel expansion of Eq. (17.4) and (17.5) gives,

$$I_f(t) = \frac{1}{2}[1 - 2J_1(\delta_0)q\sin\omega t + 2J_2(\delta_0)u\cos 2\omega t + \ldots]; \tag{17.6}$$

$$I_{fr} = \frac{1}{2}[1 - 2J_1(\delta_0)v\sin\omega t + 2J_2(\delta_0)u\cos 2\omega t + \ldots]. \tag{17.7}$$

The normalized Stokes parameters of the light scattered by the sample (u,q,v) can thus be obtained from synchronously-detected lock-in amplifier signals at the first harmonic of the signal at the chopper frequency V_{1fc} (the 'zeroth' harmonic, or the dc signal level), and at the first and second harmonics of the signal at the PEM frequency V_{1fp} and V_{2fp} respectively. The experimentally measurable waveform in terms of the detected voltage signal is

$$V(t) = V_{1fc} + \sqrt{2}V_{1f}\sin\omega t + \sqrt{2}V_{2f}\cos 2\omega t, \tag{17.8}$$

which takes into account the rms nature of lock-in detection [5]. Applying Eq. (17.8) to the set-up with detection waveplate in the analyzer arm (Eq. (17.6)) gives

$$V_{1fc} = \frac{I}{2}k; \tag{17.9}$$

$$\sqrt{2}V_{1f} = -IkJ_1(\delta_0)q; \tag{17.10}$$

$$\sqrt{2}V_{2f} = IkJ_2(\delta_0)u, \tag{17.11}$$

where k is an instrumental constant, the same for all equations. The normalized linear polarization Stokes parameters q and u are then found from

$$q = \frac{V_{1fp}}{\sqrt{2}J_1(\delta_0)V_{1fc}}; \tag{17.12}$$

$$u = \frac{V_{2fp}}{\sqrt{2}J_2(\delta_o)V_{1fc}}. \tag{17.13}$$

Comparing Eqs. (17.8) and (17.7) when the detection quarter wave plate is removed yields

$$V_{1fc} = \frac{I}{2}k; \tag{17.14}$$

$$\sqrt{2}V_{1f} = -IkJ_1(\delta_0)v, \tag{17.15}$$

and the circular polarization Stokes parameter v is then found from,

$$v = \frac{V_{1fp}}{\sqrt{2}J_1(\delta_o)V_{1fc}}. \tag{17.16}$$

The negative signs in Eqs. (17.10) and (17.15) are dropped in the final equations as positive voltages are measured; instead, the sign of the Stokes parameters is determined from the lock-in amplifier phase of the detected signals.

The measured Stokes parameters thus obtained allow for complete characterization of the polarization of the light exiting the sample. The orientation of the plane of linear polarization γ can be calculated as,

$$\gamma = \tan^{-1}\left(\frac{u}{q}\right). \tag{17.17}$$

Based on the known input plane of the incident linear polarization γ_i, the optical rotation produced by the sample can be calculated as

$$\alpha = \gamma - \gamma_i. \tag{17.18}$$

The optical rotation can be related the concentration of optically active constituents, for example through the simple relationship $\alpha = R \cdot C \cdot \langle L \rangle$ of Eq. (17.1), however, in the case of scattering media such as tissue, the ambiguity of the average optical pathlength $\langle L \rangle$ may necessitate more complex analysis (section 17.5).

Measured glucose-induced optical rotation in scattering phantoms (1.4 μm diameter polystyrene microspheres in water, resulting scattering coefficient of μ_s = 28 cm^{-1} as calculated from Mie theory) with added glucose concentrations down to physiological levels (5 to 10 mM) are shown in Fig. 17.2. These measurements were performed in the forward direction ($\theta = 0^\circ$ in Fig. 17.1) through 1 cm of scattering material (1cm $\times$1cm $\times$ 4cm quartz cuvette containing the turbid chiral suspensions). A moderate scattering level was selected ($\sim$1/3 of biological tissue in the visible-near IR range [14]), as depolarization in the forward direction through thick samples (1 cm in this case) is quite severe, limiting the accuracy with which small optical rotation values due to small glucose levels can be accurately measured. While the degree of surviving polarization, and thus the accuracy of optical rotation determination, can be greater at other detection directions θ, the contribution of scattering-induced optical rotation can also be greater, masking the small chirality-induced optical rotation due to glucose (see section 17.5). The ways to decouple these glucose-induced and scattering-induced polarization effects, and various trade-offs associated with optimum detection geometry, are discussed elsewhere in this chapter. Nevertheless, the results in Fig.17.2 demonstrate the potential for measuring very small optical rotations (milli-degree levels) in turbid media using the sensitive polarization modulation / synchronous lock-in detection experimental platform.

Measurements of glucose induced optical rotation (1.2 M glucose concentration) as a function of the scattering coefficient are shown in Fig. 17.3. As in Fig.17.2, these measurements were performed in the forward direction through a similar quartz cuvette. The optical rotation increases with increasing scattering due to the increase in average optical pathlength ($\langle L \rangle$ in Eq. (17.1)) produced with additional scattering events. However, the optical rotation begins to plateau and eventually decrease as the medium becomes highly scattering ($\mu_s > 40$ cm^{-1}). This is due to the eventual depolarization caused by multiple scattering. The light that has lost its polarization no longer contributes to the net optical rotation and as a result there is a reduction in optical rotation. The implication to glucose monitoring is that measurement sites and geometries must be chosen such that a reasonably large portion of the light remains polarized to contribute to the net optical rotation. In addition, as discussed later (section 17.5), the measurement geometry also plays a large role in the scattering-induced optical rotation which must also be taken into account.

Although the Stokes vector description can yield sample-specific information as above, the measured and derived results also depend on the state of the input light (as evident from the basic mathematical set-up of the problem, $\mathbf{S}_{sample} = \mathbf{M}_{sample} \cdot$

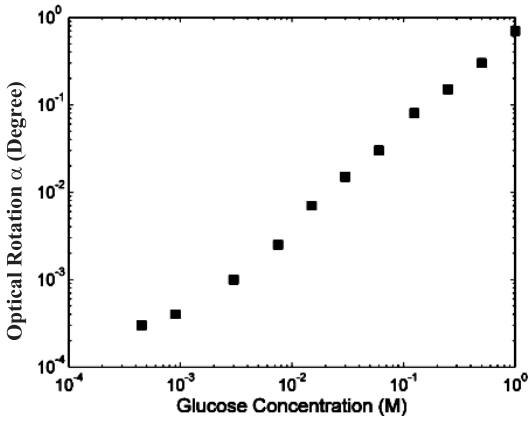

FIGURE 17.2: Logarithmic plot of optical rotation as a function of glucose concentration in scattering media (1.4 μm diameter polystyrene microspheres in water, $\mu_s \sim$28 cm^{-1}) down to physiological glucose levels. Measurements were performed in the forward direction ($\theta = 0^\circ$) through 1 cm of turbid media in a quartz cuvette (adapted from [6]).

$\mathbf{S}_{input}$). Arguably a more 'intrinsic' descriptor of sample properties, independent of the input polarization state and representing the true sample polarization transfer function, is its Mueller matrix **M**. Fortunately, the described PEM-based experimental platform can also perform sensitive Mueller polarimetry, by measuring the output Stokes vectors for four incident polarization states: input linearly polarized light at 0°, 45°, and 90°, and input circularly polarized light. The four input states are denoted with the subscripts H (**h**orizontal), P (45°), V (**v**ertical), and R (**r**ight circularly polarized, although left incidence can be used as well, resulting only in a sign change). The elements of the resulting 4 measured Stokes vectors can be combined to yield the sample Mueller matrix as,

$$\mathbf{M}(i,j) = \begin{pmatrix} \frac{1}{2}(I_H + I_V) & \frac{1}{2}(I_H - I_V) & I_P - \mathrm{M}(1,1) & I_R - \mathrm{M}(1,1) \\ \frac{1}{2}(Q_H + Q_V) & \frac{1}{2}(Q_H - Q_V) & Q_P - \mathrm{M}(2,1) & Q_R - \mathrm{M}(2,1) \\ \frac{1}{2}(U_H + U_V) & \frac{1}{2}(U_H - U_V) & U_P - \mathrm{M}(3,1) & U_R - \mathrm{M}(3,1) \\ \frac{1}{2}(V_H + V_V) & \frac{1}{2}(V_H - V_V) & V_P - \mathrm{M}(4,1) & V_R - \mathrm{M}(4,1) \end{pmatrix} \tag{17.19}$$

where the indices $i, j = 1,2,3,4$ denote rows and columns respectively. As will be described later, the measured Mueller matrix can also be used to quantify the optical rotation produced by a sample, which can be related to the concentration of optically active molecules such as glucose.

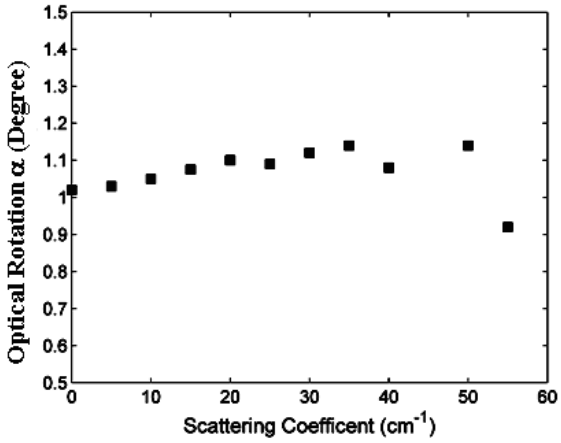

FIGURE 17.3: Measured optical rotation with 1.2 M glucose as a function of scattering coefficient (1.4 μm diameter microspheres) in the forward direction ($\theta = 0^\circ$) through 1 cm of turbid media contained in a quartz cuvette (adapted from [15]).

In summary, the described experimental approach based on polarization modulation and synchronous detection is suitable for sensitive polarimetric detection in turbid media. Several fundamental studies of turbid chiral polarimetry have been published [5–10, 15]. Continuing experimental improvements to maximize detection sensitivity to small glucose levels, such as the use of balanced detection, geometrical optimization, and spectroscopic extension are ongoing. We now turn to the equally challenging problems of accurately modeling the polarization signals in turbid media, both in the *forward* (section 17.3) and *inverse* senses (section 17.4).

17.3 Polarimetry in turbid media: accurate forward modeling using the Monte Carlo approach

To aid in the investigation of polarimetry-based glucose monitoring in biological tissue, accurate *forward* modeling is enormously useful for gaining physical insight, designing and optimizing experiments, and analyzing / interpreting the measured data. The glucose polarimetry modeling is particularly formidable, as there are several complex polarization effects occurring in tissue simultaneously, and the potential for losing the small glucose-induced polarization signal, or misinterpreting it, is high. The use of electromagnetic theory with Maxwell's equations is the most rigorous and best-suited method for polarimetry analysis, at least in clear media with well-defined optical interfaces; however, due to the ensuing complexity, the

Maxwell's equations approach for polarized light propagation in turbid media is impractical in most circumstances [16]. Instead, light propagation through multiply scattering media is often modelled through transport theory; however, transport theory and its simplified variant, the diffusion equation, are both intensity-based techniques, and hence typically neglect polarization [17, 18]. A more general and robust approach is the Monte Carlo (MC) technique, with its advantage of applicability to arbitrary geometries and arbitrary optical properties. The first Monte Carlo models were also developed for intensity calculations only and neglected polarization, the most commonly used being the share-ware code of Wang *et al.* [19]. More recently, a number of implementations have incorporated polarization into their Monte Carlo models by keeping track of the Stokes vectors of propagating photon packets [15, 20–25].

In polarization-sensitive Monte Carlo modelling, it is assumed that scattering events occur independently of each other and have no coherence effects. The position, propagation direction, and polarization of each photon are initialized and modified as the photon propagates through the sample. The photon's polarization, with respect to a set of arbitrary orthonormal axes defining its reference frame, is represented as a Stokes vector **S** and polarization effects are applied using medium Mueller matrices **M**. The photon propagates in the sample between scattering events a distance sampled from the probability distribution $\exp(-\mu_t d)$, where the extinction coefficient μ_t is the sum of the absorption μ_a and scattering μ_s coefficients and d is the distance travelled by the photon between scattering events. Upon encountering a scattering event, a scattering plane and angle are statistically sampled based on the polarization state of the photon and the Mueller matrix of the scatterer. The photon's reference frame is first expressed in the scattering plane and then transformed to the laboratory (experimentally observable) frame through multiplication by a Mueller matrix calculated through Mie scattering theory [26]. Upon encountering an interface (either an internal one, representing tissue domains of different optical properties, or an external one, representing external tissue boundary), the probability of either reflection or transmission is calculated using Fresnel coefficients [15]. As no interference effects are considered, the final Stokes vector for light exiting the sample in a particular direction are computed as the sum of all the appropriate directional photon sub-populations. Various quantities of interest such as detected intensities, polarization (Stokes vectors) properties, average pathlengths, and so forth, can be quantified once sufficient number of photon (packets) have been followed and tracked to generate statistically acceptable results (typically $10^7 - -10^9$ photons) [15]. We and others have performed a number of Monte Carlo simulation studies to gain insight into the behavior of polarized light in tissues and tissue-like media [15, 20–25, 27].

However, most current Monte Carlo models for polarized light propagation do not fully simulate all of the polarization-influencing effects of tissue. This is because modeling *simultaneous* polarization effects is difficult, especially in the presence of multiple scattering. Yet in biological tissue, effects such as optical activity due to chiral molecules (*e.g.*, glucose and proteins) and linear birefringence due to anisotropic tissue structures (*e.g.*, collagen, elastin, and muscle fibers), must be incorporated into

the model in the presence of scattering. This is particularly important in glucose polarimetry, as many tissues at accessible anatomical sites (finger, lip, ear lobe) exhibit anisotropic structures manifesting itself as linear birefringence (also known as linear retardance). Fortunately, there exits a method to simulate simultaneous polarization effect in *clear* media through the so-called N-matrix formalism, and applying this approach in tissue-like media *between* scattering events can yield an accurate Monte Carlo tissue polarimetry model [27].

Briefly, the Mueller matrices for linear birefringence and optical activity are known and can correctly model these effects individually; the problem arises in applying the combined effect when both are exhibited simultaneously, especially in the presence of scattering by the sample. Matrix multiplication is in general *not* commutative, thus different orders in which these effects are applied will have different effects on the polarization. Ordered multiplication in fact does not make physical sense, as these occur simultaneously and not one after the other as sequential multiplication implies. This necessitates the combination of the effects into a single matrix describing them simultaneously. The N-matrix algorithm was first developed by Jones [28], however, a more thorough derivation is provided in Kliger *et al.* [29]. The issue of non-commutative matrices is overcome by representing the matrix of the sample as an exponential function of a sum of matrices, where each matrix in the sum corresponds to a single optical polarization effect. This overcomes the ordering issue, as matrix addition (summation) is always commutative, and applies to differential matrices representing the optical property over an infinitely small optical pathlength. Derived from their parent matrices, these are known as N-matrices. The differential N-matrices corresponding to each optical property exhibited by the sample can then be summed to express the combined effect. The formalism is expressed in terms of 2×2 Jones matrices applicable to clear non-depolarizing media, rather than the more commonly used 4×4 Mueller matrices previously discussed. However, a Jones matrix can be converted to a Mueller matrix, provided there are no depolarization effects, as described in Schellman and Jensen [30]. This is indeed applicable to our Monte Carlo model, as depolarization is caused by the (multiple) scattering events, and no depolarization effects occur *between* the scattering events.

Results from validation experiments are shown in Fig. 17.4, where measurements from phantoms with controllable scattering, linear birefringence, and optical activity were used to test the developed model [27]. The plot shows the change in the normalized Stokes parameter $q = Q/I$ with increasing birefringence, measured in phantoms and calculated from the MC model in the forward direction of a $1 \times 1 \times 1$ cm^3 sample with input circularly polarized light. Good agreement between the developed Monte Carlo model and controlled experimental results is seen. As the input light is transferred from circular to linear polarization due to the increasing sample birefringence (the sample in effect acting like a turbid wave-plate), optical rotation due to optical activity of dissolved sugar (the use of sucrose instead of glucose was dictated by experimental considerations of sample preparation) is seen as an increase in parameter q. No such effect is seen in the absence of chirality. While these validation experiments were carried out with much higher levels of optical activity than those present physiologically, the model can be used to simulate physiologically relevant levels as

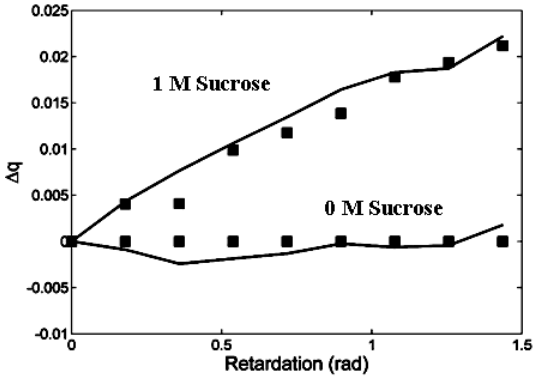

FIGURE 17.4: Experimental measurements (squares) and Monte Carlo calculations (lines) of the change in the normalized Stokes parameter q with and without optical activity (dotted lines and circles) in the forward ($\theta = 0^\circ$) detection geometry with input circularly polarized light and a fixed scattering coefficient of $\mu_s = 60$ cm^{-1}. Birefringence was varied from $\delta = 0$ to 1.4364 rad ($\Delta n = 0$ to 1.628×10^{-5}) and the magnitude of optical activity was $\chi = 1.965^\circ$ cm^{-1}, corresponding to a 1 M sucrose concentration. Refractive index matching effects have been ignored in the MC simulations (adapted from reference [27]).

discussed in the spectral chemometrics section (section 17.6). Lower levels of optical activity can be handled with noise reduction methods such as smoothening or interpolating, to deal with statistical noise due to discrete nature of the Monte Carlo model.

Figure 17.5 plots the Monte Carlo calculated normalized Stokes parameters with fixed optical activity and increasing birefringence similar to Fig. 17.4, except now that several levels of glucose are now simulated (0 M, 1 M, and 10 M). As we are interested in the optical activity-induced effects of glucose only, the glucose-induced refractive index matching effects [7] have been ignored in these MC simulations. Similar to the previous results, the sample was a $1 \times 1 \times 1$ cm^3 cube and the input light was circularly polarized. The large magnitude birefringence effects on the parameters u and v are quite evident due to the transfer from the input linear to circularly polarized light; however, the optical activity induced effects are small and only evident for the parameter q. The simulated levels of birefringence (0 to 1.5 rad) are actually somewhat lower than those present in most tissue [27]; however, the levels of glucose are several orders of magnitude higher than that present in biological tissue. The glucose effects on the resulting Stokes parameters for this geometry and sample properties are not large.

To conclude the forward-modeling section, we have described and validated a comprehensive polarization-sensitive Monte Carlo model capable of simulating complex tissue polarimetry effects, including simultaneous optical activity and birefrin-

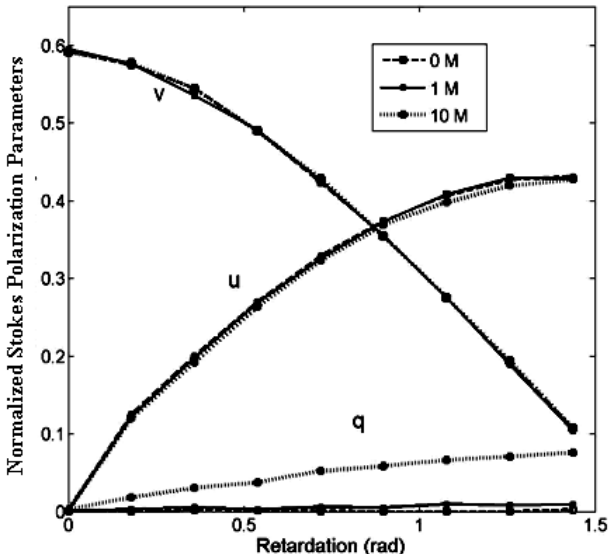

FIGURE 17.5: Monte Carlo calculations with optical activity $\chi = 0^\circ$ cm^{-1} (dashed lines), $\chi = 0.8194^\circ$ cm^{-1} (solid lines), and $\chi = 8.194^\circ$ cm^{-1} (dotted lines) corresponding to 0 M, 1 M, and 10 M glucose concentrations respectively. The normalized Stokes parameters are plotted in the forward detection geometry with input circularly polarized light and a fixed scattering coefficient of 60 cm^{-1} for all glucose concentrations. Birefringence is varied from $\delta = 0$ to 1.4364 rad ($\Delta n = 0$ to 1.628×10^{-5}). Only a small chirality-induced change in q is apparent. Glucose-induced refractive index matching effects have been ignored in the MC simulations (adapted from reference [27]).

gence in the presence of scattering. The refinement and use of this model is ongoing, specifically as applied to the glucose detection problem, viz. detection geometry optimization, pathlength / sampling volume quantification, and evaluation of spectral polarimetry. Some of these studies are described subsequently.

17.4 Tackling the inverse problem: polar decomposition of the lumped Mueller matrix to extract individual polarization contributions

Having established the ability to accurately measure and model turbid polarimetry signals in the *forward* sense, we now turn to the complicated *inverse* problem of separating out the constituent contributions from simultaneous optical effects. That is, given a particular Mueller matrix obtained from an unknown complex system such as biological tissue with some glucose level, can it be analyzed to extract constituent polarization contributions? This is a formidable task because when many optical polarization effects are simultaneously occurring in the sample (as is the case for biological tissue that often exhibit depolarization, linear birefringence and optical activity), the resulting elements of the net Mueller matrix reflect several 'lumped' effects, thus hindering their unique interpretation. Mueller matrix decomposition methodology that enables the extraction of the individual intrinsic polarimetry characteristics may be used to address this problem [31]. Preliminary results on the use of this approach for extraction of the component of optical rotation arising purely due to circular birefringence (caused by glucose and other optically active molecules) by decoupling the other confounding effects in a complex turbid medium are encouraging, as summarized in this section.

Polar decomposition of an arbitrary Mueller matrix $\mathbf{M}$ into the product of three elementary matrices representing a depolarizer ($\mathbf{M}_\Delta$), a retarder ($\mathbf{M}_R$) and a diattenuator ($\mathbf{M}_D$) can be accomplished via [31]

$$\mathbf{M} = \mathbf{M}_\Delta \cdot \mathbf{M}_R \cdot \mathbf{M}_D. \tag{17.20}$$

The validity of this decomposition procedure was first demonstrated in optically *clear* media by Lu and Chipman [31]. As mentioned before in the context of forward modelling with the N-matrix approach, matrix multiplication is generally not commutative; thus the order of these elementary matrices is important. It has been shown previously that the order selected in Eq. (17.20) always produces a physically realizable Mueller matrix; it is thus favorable to use this order of decomposition when nothing is known *a priori* about an experimental Mueller matrix [32].

The three basis Mueller matrices thus determined can then be further analyzed to yield a wealth of independent constituent polarization parameters. Specifically, diattenuation (D, differential attenuation of orthogonal polarizations for both linear and circular polarization states), depolarization coefficient (Δ, linear and circular), linear retardance (δ, difference in phase between two orthogonal linear polarization, and its orientation angle Θ), and circular retardance or optical rotation (ψ, difference in phase between right and left circularly polarized light), can be determined from the decomposed basis matrices [31,33].

Proceeding as outlined above, the magnitude of diattenuation (D) can be deter-

mined as

$$D = \{1/\mathrm{M}_D(1,1)\} \times [\{\mathrm{M}_D(1,2)\}^2 + \{\mathrm{M}_D(1,3)\}^2 + \{\mathrm{M}_D(1,4)\}^2]^{1/2}. \quad (17.21)$$

Here $\mathrm{M}(i,j)$ are the elements of the 4×4 Mueller matrix $\mathbf{M}$. The coefficients $\mathrm{M}_D(1,2)$ and $\mathrm{M}_D(1,3)$ represents linear diattenuation for horizontal (vertical) and +45° (-45°) linear polarization respectively, and the coefficient $\mathrm{M}_D(1,4)$ represents circular diattenuation.

Turning to depolarization, the diagonal elements of the decomposed matrix $\mathbf{M}_\Delta$ can be used to calculate the depolarization coefficients ($\mathrm{M}_\Delta(2,2)$, $\mathrm{M}_\Delta(3,3)$ are depolarization coefficients for incident horizontal (or vertical) and 45° (or $-45°$) linearly polarized light, and $\mathrm{M}_\Delta(4,4)$ is the depolarization coefficient for incident circularly polarized light]. The net depolarization coefficient Δ is defined as

$$\Delta = 1 - |\mathrm{Tr}\,\mathbf{M}_\Delta - 1|/3. \quad (17.22)$$

Note that this definition of depolarization coefficient is different from the conventional Stokes parameter-based definition of degree of polarization $(Q^2 + U^2 + V^2)^{1/2}/I$. The later represents the value of degree of polarization resulting from several lumped polarization effects, and also depend on the incident Stokes vector. In contrast, the depolarization coefficient (Δ) defined by Eq. (17.22) represents the pure depolarizing transfer function of the medium.

Finally, the following analysis can be performed on the retardance matrix $\mathbf{M}_R$. This matrix can be further expressed as a combination of a matrix for a linear retarder (having a magnitude of linear retardance δ, its retardance axis at angle Θ with respect to the horizontal) and a circular retarder (optical rotation with magnitude of ψ) [33]. Using the known functional form of the linear retardance and optical rotation matrices, the values for optical rotation ψ) and linear retardance δ can be determined from the elements of the matrix $\mathbf{M}_R$ as [33]

$$\psi = \tan^{-1}\{[\mathrm{M}_R(3,2) - \mathrm{M}_R(2,3)]/[\mathrm{M}_R(3,2) - \mathrm{M}_R(2,3)]\}; \quad (17.23)$$

$$\delta = \cos^{-1}\{[(\mathrm{M}_R(2,2) + \mathrm{M}_R(3,3)^2 + (\mathrm{M}_R(3,2) + \mathrm{M}_R(2,3)^2]^{1/2} - 1\}. \quad (17.24)$$

Note that there are important differences between the optical rotation ψ defined through Eq. (17.23) and the rotation of the Stokes linear polarization vector α defined through Eqs. (17.17) and (17.18) of section 17.2. The parameter α represents the net change in the orientation angle of the linear polarization vector. In addition to rotation due to circular birefringence, this may also have contributions from several other confounding factors like the scattering induced rotation and the rotation of the polarization ellipse resulting from linear birefringence and its orientation. In contrast, the parameter ψ represents the component of optical rotation that is purely due to the circular birefringence property of the medium (introduced by the presence of chiral substances such as glucose).

The validity of the matrix decomposition approach summarized in Eqs. (17.20)–(17.24) in complex turbid media was tested with both experimental (section 17.2)

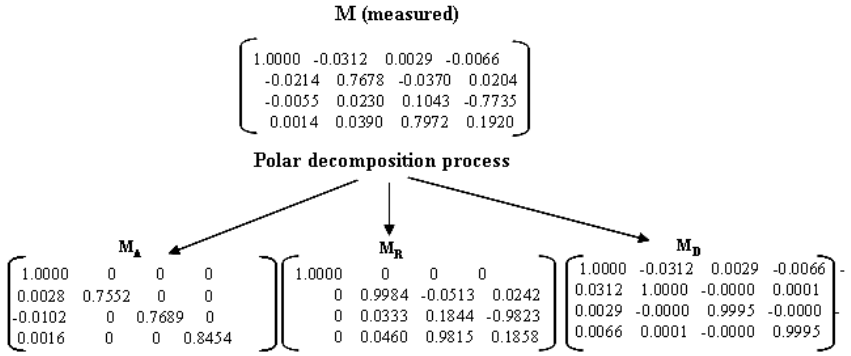

FIGURE 17.6: The experimentally recorded Mueller matrix and the decomposed matrices for a birefringent (extension = 4 mm), chiral (concentration of sucrose = 1 M), turbid ($\mu_s = 30$ cm^{-1}, $g = 0.95$) phantom. The Mueller matrix was measured in the forward direction through the 1 cm thickness.

and MC-simulated (section 17.3) Mueller matrices, whose constituent properties are known and user-controlled *a priori*.

In the experimental studies, a PEM-based polarimeter [5, 27] (section 17.2) was used to record Mueller matrices in the forward detection geometry (sample thickness 1 cm, detection area of 1 mm^2 and an acceptance angle $\sim 18^\circ$ around the forward directed ballistic beam were used) from polyacrylamide phantoms having strain-induced linear birefringence, sucrose-induced optical activity, and polystyrene microspheres-induced scattering. The Mueller matrix was generated using standard relationships between its sixteen elements and the measured output Stokes parameters $[I\ Q\ U\ V]$ for each of the four input polarization states (Eq. (17.19)) [34, 35].

Figure 17.6 shows the experimentally recorded Mueller matrix and the corresponding decomposed depolarization ($\mathbf{M}_\Delta$), retardance ($\mathbf{M}_R$) and diattenuation ($\mathbf{M}_D$) matrices. These results are from a solid polyacrylomide phantom that mimics the complexity of biological tissues, in that it exhibits birefringence (extension 4 mm for strain applied along the vertical direction), chirality (concentration of 1 M of sucrose corresponding to magnitude of optical activity per unit length of $\chi = 1.965^\circ$ cm^{-1} was used here instead of glucose for practical reasons of phantom construction), and turbidity (1.4 μm diameter polystyrene microspheres in water, resulting in a scattering coefficient of μ_s = 30 cm^{-1} and anisotropy parameter $g = 0.95$). The measurement was performed in the forward direction ($\theta = 0^\circ$) through a 1 cm$\times$1 cm$\times$4 cm phantom. Note the complicated nature of the lumped Mueller matrix and the relatively unequivocal nature of the three basis matrices derived from the decomposition process. Eqs. (17.21)–(17.24) were then applied on the decomposed basis matrices to retrieve the individual polarization parameters (diattenuation D, linear retardance δ, optical rotation ψ and depolarization coefficient Δ). The determined values for these are listed in Table 17.1.

TABLE 17.1: Comparison of the polarization parameters derived via Eqs. (17.21)–(17.24) under the same conditions as in Fig. 17.6

Parameters	Estimated value (from $\mathbf{M}_\Delta$, $\mathbf{M}_R$, $\mathbf{M}_D$)	Expected value
D	0.032	0
δ	1.384 rad	1.345 rad
ψ	2.04°	2.07°
Δ	0.790	0.806

The comparison of the derived and the input control values for the polarization parameters reveals several interesting trends. The expected value for diattenuation D is zero, whereas the decomposition method yields a small but non-zero value of $D = 0.034$. Scattering induced diattenuation that arises primarily from singly (or weakly) scattered photons [33], is not expected to contribute to the non-zero value for D because multiply scattered photons are the dominant contributor to the detected photons in the forward detection geometry. Presence of small amount of dichroic absorption (at the wavelength of excitation $\lambda = 632.8$ nm) due to anisotropic alignment of the polymer molecules in the polyacrylamide phantom may possibly contribute to this slight non-zero value for the parameter D.

The agreement in the linear retardance value of this turbid phantom ($\delta = 1.384$ rad) and that for a clear (μ_s = 0 cm^{-1}, extension = 4 mm) phantom (δ=1.345 rad) is quite reasonable. The Mueller-matrix derived value of optical rotation $\psi = 2.04°$ of the turbid phantom was, however, slightly larger than the corresponding value measured from a clear phantom having the same concentration of sucrose ($\psi_0 = 1.77°$). This small increase in the ψ value in the presence of turbidity is likely due to an increase in optical pathlength engendered by multiple scattering. Indeed, the value for ψ, calculated using the optical rotation value for the clear phantom ($\psi_0 = 1.77°$) and the value for average photon pathlength ($\langle L \rangle = 1.17$ cm, determined from Monte Carlo simulations, see section 17.5) $\psi = \psi_0 \langle L \rangle = 2.07°$ was reasonably close to the Mueller matrix derived value (ψ = 2.04°). To account for the contraction of the phantom due to longitudinal stretching, the thickness of the scattering medium was taken to be 0.967 cm (reduction in thickness at 4 mm extension using the Poisson ratio ~ 0.33 of polyacrylamide [36]) instead of 1 cm for the calculation of average photon pathlength. The overall slight lower experimental optical rotation values of the phantoms as compared to that expected for concentration of sucrose of 1 M (the experimental value of $\psi_0 = 1.77°$ for the clear phantom as compared to $\psi_0 = \chi\, L = 1.90°$, expected for path length of $L = 0.967$ cm and $\chi = 1.965°$ cm^{-1}) possibly arises due to an uncertainty in the concentration of sucrose during the process of fabrication of the phantom.

Finally, the calculated decomposition value of total depolarization of $\Delta = 0.79$ seems reasonable, although this is harder to compare with theory (there is no direct link between the scattering coefficient and resultant depolarization). The value

shown in the theoretical comparison column of the Table was determined from the Monte Carlo simulation as described in the previous section. The resultant agreement in the depolarization values is excellent. It is worth noting that decomposition results for an analogous purely depolarizing phantom (same turbidity, no birefringence nor chirality, results not shown) were within 2% of the above Δ values. This self-consistency implies that decomposition process successfully decouples the depolarization effects due to multiple scattering from optical rotation and retardation effects, thus yielding accurate and quantifiable estimates of the δ and ψ parameters in the presence of turbidity.

In order to gain additional quantitative understanding of the dependence of the estimated value for optical rotation ψ on the propagation path of multiply scattered photons, Mueller matrices were generated using Monte Carlo simulations for transmitted light (1 cm thick sample as before), collected at different spatial positions at the distal face of the scattering medium. Decomposition analysis was then performed on these Monte Carlo generated Mueller matrices. Figure 17.7 displays the variation of the parameter ψ of transmitted light as a function of distance from ballistic beam position at the distal face of a birefringent (linear retardance of δ = 1.35 radian for optical pathlength of 1 cm) turbid medium ($\mu_s = 30$ cm^{-1}, $g = 0.95$). The axis of linear birefringence was kept along the vertical direction ($\Theta = 90^\circ$) in the simulations and the different spatial positions were perpendicular to the direction of the axis of linear birefringence. The results are shown for two different values of optical activity ($\chi = 0.0820$ and 0.1640° cm^{-1}, corresponding to 100 mM and 200 mM concentration of glucose, respectively).

As one would expect, the Mueller-matrix derived values for ψ increase with increasing average photon pathlength and the values are also reasonably close to those calculated using the linear relationship ($\psi = \chi \times$ average photon pathlength). Note that the average path length has contributions from both the polarization preserving and the depolarized photons. The fact that the propagation path of the polarization preserving photons (which would show experimentally detectable optical rotation) are shorter than the average photon path length of light exiting the scattering medium [37], should account for the slightly lower value for the Mueller-matrix derived ψ (particularly at larger off-axis distances).

The results of the experimental studies on phantoms having varying optical properties and the corresponding results of Monte Carlo generated Mueller matrices demonstrate that decomposition of Mueller matrix can be used for simultaneous determination of the intrinsic values for optical rotation (ψ) and linear retardance (δ) of a birefringent, chiral, turbid medium. For conceptual and practical reasons, the extension of this methodology to backward detection geometry is warranted. This work is currently ongoing in our laboratory.

To summarize, we have described a theoretical approach for solving the inverse problem in turbid polarimetry. The Mueller matrix decomposition methodology allows the extraction of the individual intrinsic polarimetry characteristics from the lumped Mueller matrix description of a complex turbid medium. Experimental and theoretical studies in complex tissue-like media for extracting the intrinsic value for optical rotation (which is related to the concentration of chiral molecules such as

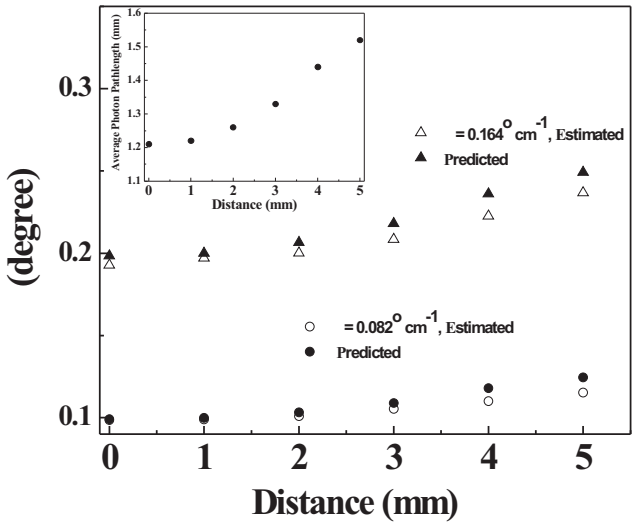

FIGURE 17.7: Variation of optical rotation parameter ψ of transmitted light as a function of distance from ballistic beam position at the distal face of a 1-cm-thick birefringent ($\delta = 1.35$ radian for optical pathlength of 1 cm) turbid ($\mu_s = 30$ cm^{-1}, $g = 0.95$) medium. The results are shown for two different values of optical activity ($\chi = 0.0820$ and 0.1640°cm^{-1}, corresponding to glucose concentrations of 100 and 200 mM, respectively). The open symbols are the ψ values estimated from the decomposition of Monte Carlo generated Mueller matrices; the solid symbols were calcultead via $\psi = \chi \times$ average photon pathlength. The inset shows the MC calculated average photon pathlength as a function of the off-axis distance (see section 17.5).

glucose) yielded very promising results. This bodes well for the potential application of this methodology for quantification of the small optical rotations due to blood glucose in diabetic patients, but this remains to be rigorously investigated. Further refinements of the highly sensitive Mueller matrix measurement set-up capable of detecting small changes in the matrix elements corresponding to the physiological glucose levels, and selection/optimization of the measurement geometry will be required. It is also pertinent to note that determination of the concentration of glucose using the measured optical rotation from a multiply scattering medium like tissue would require additional quantitative information on the pathlength distributions of polarization preserving and depolarized photon populations. Further, the use of single-wavelength measurements is unlikely to yield unequivocal results in real tissues, and the use of multi-spectral / spectroscopic turbid polarimetry will be

essential. The following two sections attempt to address some of these challenges.

17.5 Monte Carlo modeling results for measurement geometry, optical pathlength, detection depth, and sampling volume quantification

One of the many advantages of a comprehensive forward model of polarized light-biological tissue interaction (section 17.3) is the ability to explore *in silico* the wide parameter space potentially available for polarimetric tissue measurements, in an effort to determine optimum geometry for glucose sensing. Another is the ability to quantify and interpret the measured parameters by examining the sampling volume probed by light, and determining the average light pathlength in interrogated tissues. In this section, we present representative results from Monte Carlo studies and selected experimental measurements that address these issues [37–39].

Unlike the previous square/rectangular sample geometries examined to date, a cylindrical tissue model is used here. This geometry is of special relevance because the curved surfaces of human anatomy such as finger or lip are of interest in optical glucose sensing. Further, sites like the finger offer the potential geometric advantage of multiple-direction detection capability (0° to 360°, compared with 0° and 180° detections for slab-like structures and 180°-only detection for semi-infinite set-ups), and may also be more practical and convenient in a clinical setting. Fortunately, the inherent flexibility of the Monte Carlo modeling platform makes the simulations of any arbitrary sample geometry equally accessible.

Utilizing the cylindrical model, the effects of detection direction on the polarimetric signal, and specifically its influence on glucose-induced optical rotation, have been investigated. Monte Carlo predictions were validated/confirmed with selected experimental measurements. For the results reported below, turbid chiral samples in the absence of birefringence were examined. The modeling geometry shown in Fig. 17.8 mimics the experimental conditions [5, 38]. A 632.8 nm horizontally polarized beam of 1 mm diameter is incident at the point O on the center of a vertically orientated cylindrical sample of 0.8 cm in diameter and 4 cm in height. The scattered photons at point P (z, θ), within acceptance angle $\phi \sim 48^\circ$ are collected and focused onto a detector of ~ 0.7 mm^2 sensing area. The detection angle varies from 0° to 180°. The vertical position of the surface detection element z ranges from -4.0 cm to $+4.0$ cm, with the signs indicating the relative position with respect to the horizontal incident plane. The samples are highly turbid media (water suspension of microspheres of different diameter) containing D-glucose, with birefringence values set to zero. The glucose concentration ranges from 0 mM to 900 mM and the scattering coefficient μ_s is varied from 93 cm^{-1} to 100 cm^{-1}, depending on glucose levels. The scattering coefficient range is chosen to approximate typical turbidity of biological tissue. In the simulations, the cylindrical sample is characterized by a set

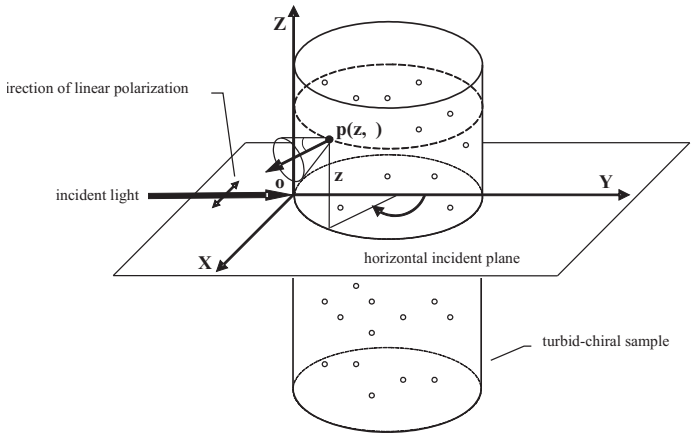

FIGURE 17.8: Cylindrical geometry used in the experiments and the Monte Carlo simulations. Linearly polarized light incidents at the point O on a vertically oriented cylindrical sample. The scattered light is collected by a small detector element at the point P (z,θ) on the surface of the cylinder with an acceptance angle ϕ. z is the distance of the detector off the horizontal incident plane ($z=0$) and θ is the detection direction (adapted from reference [37]).

of surface elements that are rectangular on the sides and triangular on the bottom and top (48 on each of the three surfaces). Additional modeling details can be found in the original articles [37 -39].

The results indicate the dramatic effects of the detection geometry. In moderately scattering samples ($\mu_s \sim 20-60$ cm^{-1}), the degree of polarization preservation decreases as one moves from forward to backward hemisphere (increasing θ), although a slight increase is seen as one approaches the exact backscattering direction ($\theta = 180^\circ$. However, for tissue-like scattering ($\mu_s sim 100$ cm^{-1}), polarization preservation can become higher when measured at higher detection angles (backwards hemisphere). For all cases, the highest polarization preservation was observed in the incident plane ($z=0$). Further, the angular dependence of optical rotation α is significant as well. Figure 17.9 shows measurement and simulation results for an *achiral* (glucose-free) highly scattering sample, where the observable α values are caused by the scattering process only (and can thus be considered as 'noise' in the context of the glucose detection problem). The effects of moving the detector off the incident plane is negligible in the forward direction, and very significant at other detection angles [Fig.17.9(a)]. Fig. 17.9(b) presents the entire modeled α-response surface in the θ, z parameter space, indicating the complicated behavior and the necessity of cautious interpretation of the measured α values — optical rotation in the presence of multiple scattering is not only caused by the chirality of

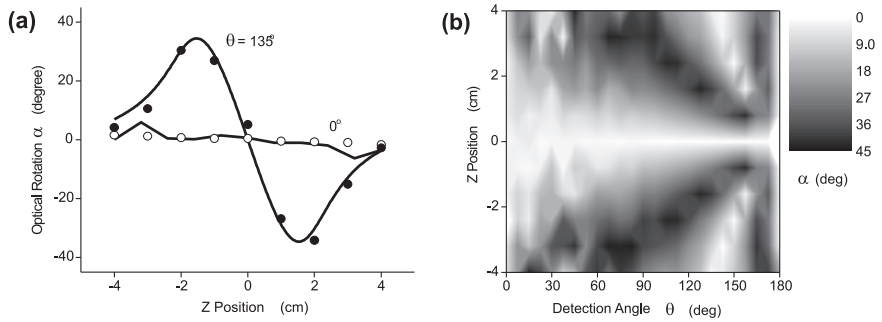

FIGURE 17.9: Optical rotation of light scattered from highly turbid ($\mu_s = 100$ cm^{-1}) achiral birefringence-free sample. (a) Simulations and measurements at $\theta = 0^\circ$ and 135° as z changes from -4 cm to 4 cm. The symbols are experimental data and the lines are Monte Carlo results. At $\theta = 135^\circ$ the optical rotation is seen to oscillate symmetrically about the incident plane with a large amplitude of $\sim 40^\circ$. This scattering-induced optical rotation is not observable at $\theta = 0^\circ$ for all examined z-values. (b) θ–z response surface of optical rotation from the MC simulation with θ changing from 0° to 180°, and z changing from -4 cm to 4 cm. In the absence of glucose, the scattering-induced optical rotation is minimal (~ 0) at $\theta = 0^\circ$ or $\theta = 180^\circ$, and everywhere in the incident plane ($z = 0$) (adapted from reference [38]).

the glucose molecules as is the case in clear-media glucometry. Note that although the scattering-induced optical rotation can be as large as 40°, it is *not* observable anywhere in the incident plane ($z = 0$), or in the in the exact forward and backwards directions ($\theta = 0^\circ$ and 180°) due to symmetry [Fig.17.9(b)]. These geometries may thus be preferable for measuring pure glucose-induced optical rotation in the highly scattering environment, subject to many other considerations (*e.g.*, ease of measurement, degree of polarization preservation).

Figure 17.10 shows the experimental optical rotation results from tissue-like turbid medium in the presence of glucose (see [38] for corresponding Monte Carlo predictions). The trends in the forward direction in the incident plane (Fig. 17.10(a)) are similar to those previously observed (Fig. 17.2), although the sample size/shape/scattering parameters are somewhat different. As one explores the backward hemisphere ($\theta = 135^\circ$ in 17.10(b)), other effects come into play. The effects of added glucose are rather modest, even in the incident plane ($z = 0$), where the interference from the scattering induced signals was shown to be minimal. Conversely, measuring off the incident plane ($z \sim 3$ mm) at this detection angle yields considerable variation in detected α values as the glucose concentration is varied. Given the large magnitude of observed changes, this is probably not caused by the chiral nature of glucose, but is likely due to the glucose refractive index matching effect [7]. That is, the glucose-caused changes in the scattering coefficient manifest themselves as large

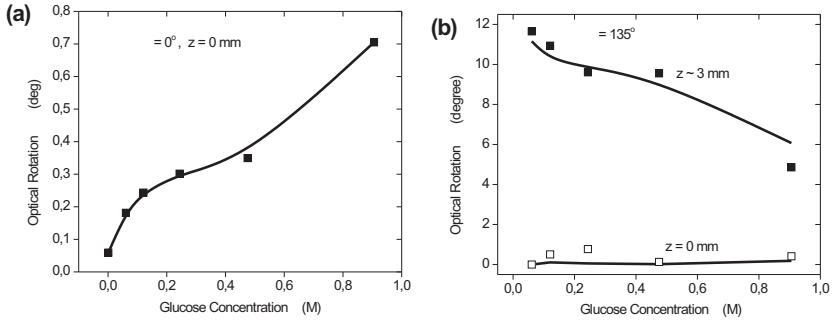

FIGURE 17.10: Optical rotation due to changes in glucose concentration in highly turbid chiral phantoms ($\mu_s = 100$ cm^{-1} in the absence of glucose, glucose concentration from 0 M to 0.9 M), measured at different detection geometries. (a) $\theta = 0^\circ$, $z = 0$ mm. A significant increase over the baseline level is observed, likely due to chiral nature of glucose. (b) $\theta = 135^\circ$, $z = 0$ mm and $z = 3$ mm. Optical rotation varies greatly with glucose concentration at $z = 3$ mm, caused by the glucose-induced refractive index matching effect; corresponding changes are not easily detectable at $z = 0$ mm. The symbols are experimental data and the lines are guides for the eye (adapted from reference [38]). Confirmatory Monte Carlo results are available in reference [38].

changes in scattering-induced optical rotation, as measured in this off-incident-plane backwards-hemisphere detection geometry. This effect may or may not prove useful as a measurable metric for glucose detection in real tissues, but clearly it must be taken into consideration in system design and data interpretation. Further studies also suggest the advantage of backward detection geometries due to better polarization preservation at high levels of (tissue-like) turbidity [38]. Clearly then, the sensitivity of turbid polarimetric glucose measurement is strongly dependent on detection geometry, and further studies are ongoing to shed additional light on this complicated issue.

Monte Carlo modeling can also offer some insights on a variety of important 'hidden' variables inherent in turbid polarimetry. Specifically, the pathlength, the detection depth, and the sampling volume of tissue-interrogating photons are all crucial for accurate glucose quantification, in that they are needed to analyze/quantify/interpret the obtained polarimetry results. However, these quantities are difficult or impossible to obtain directly from experiments. The complicated zig-zag nature of photon paths in multiply scattering media necessitates the use of statistical models such as the Monte Carlo approach. Here we show representative results for pathlength distribution studies of linearly polarized photons incident onto a cylindrical turbid samples ($\mu_s \sim 100$ cm^{-1}) [37]. In the simulations, the collected photons are binned based on

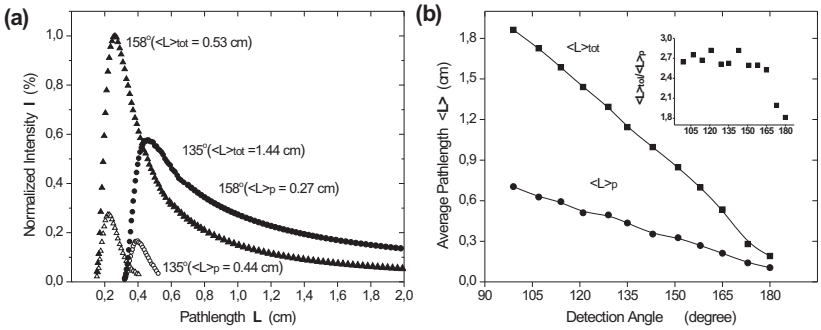

FIGURE 17.11: MC-derived pathlength distribution of photons within the incident plane ($z = 0$) at backwards detection angles ($\theta > 90^\circ$). (a) typical pathlength distributions of the polarization-maintaining photon subpopulations (hollow symbols) and the whole photon population detected at $\theta = 135^\circ$ and 158°. The average pathlength decreases with detection angle and the intensity increases with detection angle (also seen at other values of θ, see reference [37]). (b) Angular dependence of average pathlenghts for both photon populations. The average pathlengths of polarization-maintaining photons $\langle L \rangle_{\rm p}$ are shorter than the corresponding $\langle L \rangle_{\rm tot}$ of the total photon field, as quantified in the figure inset (adapted from reference[37]).

the number of scattering events N they experienced within the sample, and their pathlength, polarization states and intensity are extracted from each bin and compared with the total (N-unresolved) averaged ones. The pathlengths of photons spread out due to multiple scattering as shown in Fig. 17.11(a). Note the relatively confined pathlength distributions of polarization-maintaining photons, with their well-defined upper limit; in contrast, the total photon fields (polarized + depolarized) exhibit a much broader pathlength distribution without a definite upper limit. It is possible to calculate the corresponding *average* pathlengths for the polarized ($\langle L \rangle_{\rm p}$) and total ($\langle L \rangle_{\rm tot}$) photon fields, by summing the weighted contribution from $N = 1$ to $N \to \infty$ (in practice, the upper limit of N was ~ 70 for $\langle L \rangle_{\rm p}$, as the surviving polarization fraction was too low for higher N). The summary results for this sample turbidity are shown in Fig. 17.11(b). The average pathlength of polarized photons $\langle L \rangle_{\rm p}$ is seen to be 2–3 times smaller than the average pathlength of all collected photons, the latter being dominated by the longer traveling photon histories. The strong angular dependence of both pathlength averages is also evident. Additional simulation results show that the change in (lowering of) the scattering coefficient μ_s, as such can be engendered by the glucose index matching effect, shortens the average photon pathlengths [37].

We have also estimated the penetration depths and sampling volumes of the polarized and depolarized light in cylindrical turbid samples, using these MC-derived

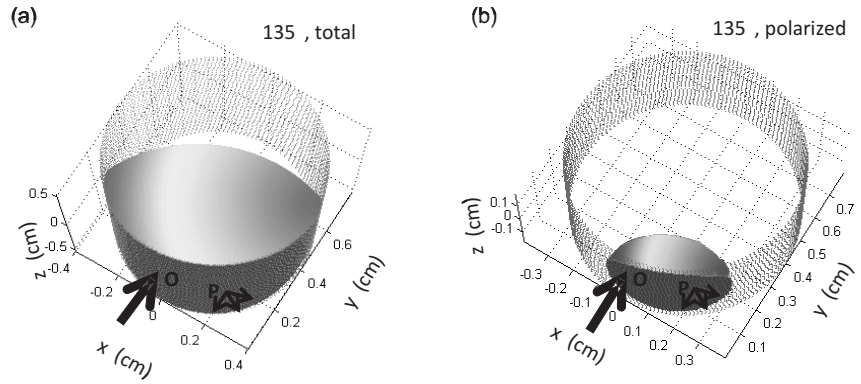

FIGURE 17.12: Optical sampling volume (the volume formed by the surface of the partial ellipsoid and the sample wall) and detection depth distribution (top view of sampling volume) at $\theta = 135^\circ$. Photons enter the cylindrical sample at O and exit at P (in the scattering plane, $z = 0$). (a) total photon population ($\langle L \rangle_{\text{tot}} = 1.44$ cm). **(b)** polarized photon subpopulation ($\langle L \rangle_{\text{p}} = 0.44$ cm). As seen, the polarized photons have smaller sampling volume and shallower detection depth than the total photon population, which is dominated by longer-travel depolarized photons (adapted from reference [39]).

pathlength distributions [39]. In this approach, the zig-zag photon path is approximated by two straight-line segments, the length sum of which is equal to the pathlength of the photon. The joint points of all the possible combination of two segments in the incident plane form an ellipse-shaped detection depth distribution and an ellipsoid-shaped sampling volume distribution. Not surprisingly, it is found that the smaller average pathlength of polarization-preserving photon subpopulation results in shallower penetration depths and smaller sampling volumes than that of all collected photons in the backward hemisphere. To quantify these trends, Fig. 17.12 shows a particular example of the two sampling volumes at a detection angle $\theta = 135^\circ$. As evident from the MC results for pathlength distributions, the detection depth and sampling volume are also strongly dependent on the detection geometry. The implication for glucose detection is that the control of spatial interrogation extent of light in tissues can be achieved (and quantified) by changing the detection angle. Small angle detection provides deeper penetrations and larger sampling volumes, whereas large angle detection (approaching the back-scattering direction at $\theta = 180^\circ$) offers near surface and localized information from within the turbid media. Any changes in glucose concentration which affects the photon pathlengths will also influence the penetration depths and sampling volumes. In concert with the polarization preservation and scattering- vs glucose-induced optical rotations results, such modelling is beginning to be applied for design considerations in a turbid polarimetry glucose detection system.

17.6 Combining intensity and polarization information via spectroscopic turbid polarimetry with chemometric analysis

Nearly all of the developing optical glucose monitoring techniques measure a signal caused not only by glucose but also by many other biological constituents. As a result, the techniques suffer in glucose specificity. The sensitivity is often lacking as well, as the signal due to glucose is generally much smaller than that due to other constituents. One method to minimize these limitations is to increase the glucose signal content via a spectral approach that collects data over a range of wavelengths. Another possibility is to utilize a dual modality optical methodology that combines the complementary strengths of the two selected techniques. Specifically, combining near-infrared (NIR) spectroscopy (see chapters 5, 6, 8 and 10 of this monograph), arguably the most promising glucose-sensing optical method to date, with spectral polarization information lends itself well to such hybrid approach, as simultaneous measurements can be made with a single polarization-sensitive optical system. In addition to potential experimental convenience and practicality, there is a scientific motivation for this spectroscopic combination. This combination exploits three optical effects of glucose: its NIR absorption spectrum as manifest in the NIR spectroscopy, its optical rotatory dispersion (ORD, also known as optical activity) as manifested in the polarimetry data, and its refractive index matching effect which can influence the results of both techniques. The last is the change in the refractive index of the media with changes in constituent glucose concentrations; this influences the scattering coefficient of the tissue [7]. For the initial simulation study described below, only the first two effects were explored (NIR absorption and ORD); unlike the index matching effect, these two are potentially specific to glucose. The effects of glucose-induced refractive index matching will be examined subsequently.

To test the combination of NIR and ORD spectroscopy for glucose concentration determination, a model of blood plasma containing glucose and plasma proteins was used to generate intensity and polarization spectra in both clear and scattering media. The effects of absorption due to water, plasma proteins, and glucose in the visible and NIR were modeled using experimental data from a number of reports [40–43]. As data for individual plasma protein absorption dispersion could not be found, the total plasma protein (albumin, globulin, and fibrinogen) absorption was used. Figure 17.13 (a) shows the resulting absorption coefficients $\mu_a(\lambda)$ per concentration of analyte and optical pathlength, given as a function of wavelength for water, total protein, and glucose. Additional details related to water displacements effects and other subtleties for accurate determination of these spectra can be found in [44]. The similarity of the glucose absorption spectrum with that for the plasma proteins should be noted, as this leads to difficultly in separating their absorption effects and corresponding concentrations. The high level of absorption due to water as the wavelength increases beyond 1400 nm also leads to difficulty as this will greatly reduce the intensity of the light exiting the sample.

The effects of optical activity due to proteins and glucose in the visible and NIR

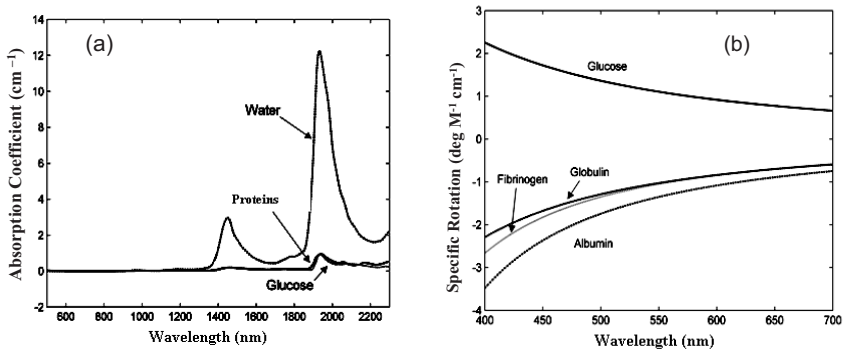

FIGURE 17.13: (a) Absorption spectra of blood plasma proteins and glucose in the visible and NIR. (b) Optical rotatory dispersion of blood plasma proteins and glucose as given by Drude's equation (Eq. (17.25)) in the visible and NIR. The parameters for the Drude's equation are: for glucose $A = 1.72 \times 10^7$ and $\lambda_c = 150$ nm, for albumin $A = -1.75 \times 10^7$ and $\lambda_c = 264$ nm, for globulin $A = -1.48 \times 10^7$ and $\lambda_c = 211$ nm, and for fibrinogen $A = -1.37 \times 10^7$ and $\lambda_c = 260$ nm (adapted from reference [46]).

were modeled using Drude's equation,

$$[\alpha]_\lambda = \frac{A}{\lambda^2 - \lambda_c^2}, \tag{17.25}$$

where $[\alpha]_\lambda$ is the specific rotation of the molecule in units of $\frac{\text{deg.}}{g/ml-dm}$ at the wavelength λ, A is constant specific to the molecule, and λ_c is the center wavelength [22]. The resulting ORD spectra are displayed in Fig. 17.13 (b), with the parameter of the Drude's equation for the plasma proteins [44] and glucose [1] shown in the figure caption. The induced rotations due to proteins and glucose have opposite signs, the proteins rotate to the left (negative sign) while glucose rotates to the right (positive sign). From the plot of the Drude's parameters it is evident that the spectral dependence for glucose and proteins, while having opposite senses of rotation, are very similar. This leads to difficultly in separating the rotation due to glucose from that due to proteins.

For clear media, the values for $\mu_a(\lambda)$ and $\alpha(\lambda)$ can be used to calculate the Mueller matrix for the sample and the resulting Stokes vector for light after propagating through the sample. For scattering media, the Monte Carlo model (section 17.3) was used to generate spectral values for the output Stokes vectors with the $\mu_a(\lambda)$ and $\alpha(\lambda)$ spectral inputs of Fig. 17.13. The turbidity of the medium was set to be $\mu_s = 60$ cm^{-1} (somewhat lower than tissue in order to reduce computational time), the sample was a $1 \times 1 \times 1$ cm^3 cube, and forward-detection geometry ($\theta = 0^\circ$) was simulated. The birefringence value was set to zero for this initial study; its effects will be investigated later. As generating the full spectrum through Monte

Carlo simulations is computationally intensive, a lookup table method was found to be useful. Here, the input values of μ_a and α are varied in regular intervals to create a table from which the spectra of the output Stokes parameters can be generated. The lookup table also allows for noise reduction, as the data can be smoothed to reduce statistical noise due to the discrete nature of the model. This is particularly important, as the simulated physiological glucose levels are small (3–17 mM), as are the resulting glucose dependent effects.

As with nearly all of the developing optical techniques, this methodology must now isolate the glucose-specific contribution from signals (Stokes vectors over many wavelengths in this case) influenced by many other confounding factors (plasma proteins and water in this case). For the lumped Mueller matrix formulation at a single wavelength, the polar decomposition method was developed (section 17.4). Here we explore the use of spectroscopic analysis of Stokes vectors via a chemometric approach. The field of chemometrics provides a number of well-developed techniques for analyzing measurements of complex chemical systems, to yield constituent concentrations or other properties of interest [45]. Most of these techniques regress one block of data, such as a set of NIR absorption spectra, to a single sample property of the sample, such as glucose concentrations, to build a predictive model. In our case, we wish to regress two blocks of spectroscopic data (NIR intensity signals — element I of the Stokes vector and ORD polarization signals—elements Q and U of the Stokes vector) to improve the predictive abilities of the chemometric model. This requires the use of multi-block chemometrics to combine two or more of the data sets into a single predictive model. For this study, multiblock partial least squares (MB-PLS) was employed as the regression technique.

The MB-PLS is based on the widely used PLS regression method. In PLS, a regression relationship is found between a descriptor block or matrix of data (in our case, a set of intensity or polarization spectra) and a response block or matrix (in our case, a set of corresponding glucose concentrations). This is achieved by decomposing both the descriptor and response blocks into so called latent variables that describe the maximum variance in the data. The regression is calculated based on how the variances in each block explain each other, in other words finding the covariance between the blocks. In situations where there is more than one descriptor block, as in this case where we have intensity and polarization measurements, a method of combining the information in both descriptor blocks must be used in order to predict the response block.

In this method the blocks are used to create a single super descriptor block as shown in Fig. 17.14, which is then regressed to the response block using PLS. The creation of this super-block involves finding the common information contained in each of the descriptor blocks, referred to as the "consensus" in the literature. In other words, the variations in the signals that are common in both descriptor blocks are identified as the consensus between the two blocks. As each block contains measurements done on the same samples, looking at the common information contained in each block can provide better predictive ability for analytes that affect both measurement techniques (as those in our plasma model do). For example, glucose (as well as plasma proteins) influences both the intensity and polarization signals caus-

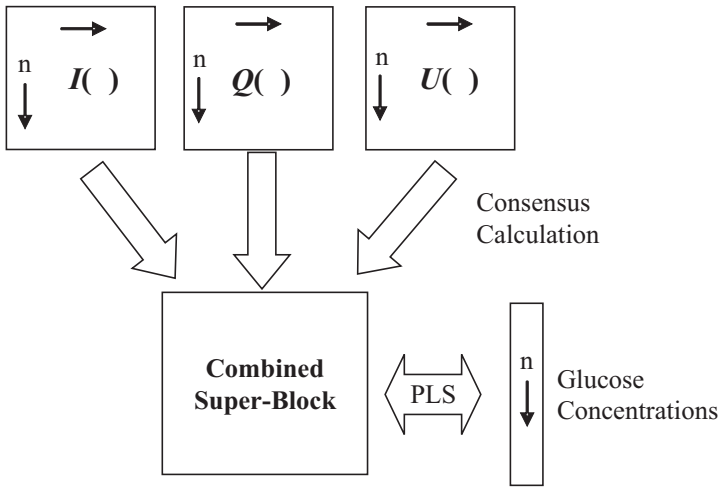

FIGURE 17.14: Schematic summarizing how multiblock partial least squares (MB-PLS) chemometric algorithm combines and regresses the generated spectroscopic intensity ($I(\lambda)$) and polarization ($Q(\lambda)$, $U(\lambda)$) data; $V(\lambda)$ was not used for regression calculations as glucose chirality does not effect circular polarization (adapted from reference [46]).

ing a common variation in both signals, and are identified in the calculation of the consensus.

Two steps are required in the development of a chemometric model: calibration and testing. In calibration, often referred to as training, a set of data (both descriptor and response blocks) is used to create the PLS model. In our case, a set of intensity and polarization spectra (descriptor blocks) as well as glucose concentrations corresponding to each spectrum (response blocks) were used to calculate the regression parameters using MB-PLS. Once the model is built in this calibration step, it must be tested with new data to ensure the validity of the model and assess its predictive ability. A new set of intensity and polarization spectra along with corresponding glucose concentrations were generated for the purposes of testing both regression techniques. The size of both the calibration and testing data sets were 400 spectra with corresponding glucose concentrations. The predictive ability of the methods can then be determined by calculating the root mean square error of prediction using the testing data set, with increasing noise added to both the training and testing spectra.

Results from predictions in both clear and scattering media are shown in Fig. 17.15. The added noise level in the Stokes vectors were taken to be small, typical to that attainable with high precision polarimetry system. Here $I(\lambda)$ was regressed individually and then combined with $Q(\lambda)$, $U(\lambda)$ and regressed using MB-PLS. The parameter $V(\lambda)$ was not included in regression as circularly polarized light is not ef-

fected by the chirality of glucose. Significant improvement in error can be seen when the intensity and polarization information are combined in both clear and scattering media. For clear media a reduction in error of approximately 25% was achieved and in scattering media a reduction in error of approximately 15% was achieved. The improvement was somewhat diminished with the addition of scattering to the model as this effectively reduces the magnitude of the polarization signals due to depolarization.

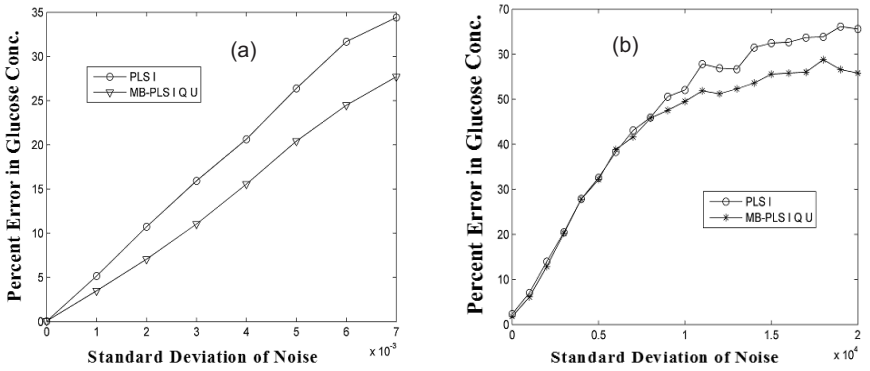

FIGURE 17.15: Percent error as a function of simulated noise in (a) clear media and (b) scattering media for $I(\lambda)$ regressed with PLS as well as $I(\lambda)$, $Q(\lambda)$, and $U(\lambda)$ combined and regressed using MB-PLS. The standard deviation of added noise differs as the spectra in (a) were calculated directly while those in (b) were generated with the Monte Carlo model (adapted from reference [46]).

A significant improvement (approximately 15%) in predictive ability is still achieved with the combination of intensity and polarization information from simulated multiple scattering media. Future work will further investigate the influence of scattering, in an effort to determine up to what level of scattering an improvement is still realized. As this rather large reduction in improvement has already been observed from clear to a scattering coefficient of 60 cm^{-1}, it would seem unlikely that predictions with more realistic tissue scattering values ($\sim$ 100 cm^{-1}) will exhibit significant improvement. However, this is yet to be determined, as smoothing or other preprocessing steps can be used to reduce the signal noise. The present results demonstrate the potential for the methodology in clear or moderately scattering biological media, such as blood plasma or extra-cellular fluid [46].

17.7 Concluding remarks on the prospect of glucose detection in optically thick scattering tissues with polarized light

In this chapter, the use of polarized light for tissue assessment has been discussed in the context of noninvasive glucose detection. Despite the inherent difficulty of polarimetric approach for examinations of complex turbid media such as tissue, reliable measurements and analyses can be performed. A variety of experimental and theoretical tools have been developed to maximize measurement sensitivity, interpret the measurement results, isolate specific polarization contributions, quantify 'hidden' important variable such as photon pathlength and sampling volume, and evaluate the validity of the spectroscopic tissue polarimetry. Specifically, a comprehensive turbid polarimetry platform had been described, comprising of a highly sensitive experimental system, an accurate forward model that can handle all the complex simultaneous polarization effects manifested by biological tissues, and an inverse signal analysis strategy that can be applied to complex tissue polarimetry data to isolate specific quantities of interest (such as small optical rotation that can be linked to glucose concentration).

Illustrative examples from tissue-simulating phantoms of increasing biological complexity have been presented, with consistent and encouraging results. The application of this methodology for glucose detection and quantification in real tissues remains to be investigated, and is currently being initiated in our laboratory. Certainly, the low physiological glucose levels, the high (and variable) levels of tissue scattering, the varying levels of tissue optical absorption, the presence of other optically-active molecules, and the confounding effects of various biological variables (pH, temperature, *etc*.) will pose significant challenges to any noninvasive glucose monitoring approach, including the one described in this chapter. Nevertheless, the turbid polarimetry progress to date bodes well for future in-vivo developments. Finally, it may come to pass that the solution for noninvasive glucose monitoring lies in combining two or more of the methods described in this monograph, judiciously combining their complementary strengths to overcome the formidable biological complexity inherent in this important clinical problem.

Acknowledgements

Our turbid polarimetry research is supported by the Natural Sciences and Engineering Research Council of Canada (NSERC). The authors would also like to thank Dr. Daniel Côté for his contributions in some of the studies discussed in this chapter.

References

[1] R. J. McNichols and G. L. Coté, "Optical glucose monitoring in biological fluids: an overview," *J. Biomed. Opt.*, vol. 5, 2002, pp. 5-16.

[2] V.V. Tuchin, L. Wang, and D.L. Zimnyakov, *Optical Polarization in Biomedical Applications*, Springer-Verlag, Heidelberg, 2006.

[3] V.V. Tuchin, *Optical Clearing of Tissues and Blood*, vol. PM 154, SPIE Press, Bellingham, WA, 2006.

[4] C.A. Browne and F.W. Zerban, *Physical and Chemical Methods of Sugar Analysis*, Wiley, New York, 1941.

[5] X. Guo, M.F.G. Wood, I.A. Vitkin, "Angular measurement of light scattered by turbid chiral media using linear Stokes polarimetry," *J. Biomed. Opt.*, vol. 11, 2006, 041105.

[6] D. Côté and I. A. Vitkin, "Balanced detection for low-noise precision polarimetric measurements of optically active, multiply scattering tissue phantoms," *J. Biomed. Opt.*, vol. 9, 2004, pp. 213-220.

[7] K.C. Hadley and I.A. Vitkin, "Optical rotation and linear and circular depolarization rates in diffusely scattered light from chiral, racemic, and achiral turbid media," *J. Biomed. Opt.*, vol. 7, 2002, pp. 291-299.

[8] I.A. Vitkin, R.D. Laszlo, and C.L. Whyman, "Effects of molecular asymmetry of optically active molecules on the polarization properties of multiply scattered light," *Opt. Exp.*, vol. 10, 2002, pp. 222-229.

[9] R.C.N. Studinski, I.A. Vitkin, "Methodology for examining polarized light interactions with tissues and tissue-like media in the exact backscattering direction," *J. Biomed. Opt.*, vol. 5, 2000, pp. 330-337.

[10] I.A. Vitkin and E. Hoskinson, "Polarization studies in multiply scattering media," *Opt. Eng.*, vol. 39, 2000, pp. 353-362.

[11] J. Badoz, M. Billardon, J.C. Canit, and M.F. Russel, "Sensitive devise to measure the state and degree of polarization of a light beam using a birefringence modulator," *J. Opt.*, vol. 8, 1977, pp. 373-384.

[12] M.P. Silverman, N. Ritchie. G.M. Cushman, B. Fisher, "Experimental configurations using optical phase modulation to measure chiral asymmetries in light specularly reflected from a naturally gyroptopic medium," *J. Opt. Soc. Am. A.*, vol. 5, 1988, pp. 1852-1863.

[13] M. Abramowitz and I. Stegun, *Handbook of Mathematical Functions with Formulas, Graphs, and Mathematical Tables*, National Institute of Standards and Technology, Washington, D.C., 1964.

[14] W.F. Cheong, S.A. Prahl, and A.J. Welch, "A review of the optical properties of biological tissues," *IEEE Journal of Quantum Electronics,* vol. 26, 1990, pp. 2166-2185.

[15] D. Côté and I.A. Vitkin, "Robust concentration determination of optically active molecules in turbid media with validated three-dimensional polarization sensitive Monte Carlo calculations," *Opt. Exp.*, vol. 13, 2005, pp. 148-163.

[16] A.J. Welch and M.J.C. van Gemert, *Optical-Thermal Response of Laser Irradiated Tissue*, Plenum Press, New York, 1995.

[17] A. J. Welch, G. Yoon, and M. J. van Gemert, "Practical models for light distribution laser-irradiated tissue," *Lasers Surg. Med., vol*. 6, 1987, pp. 488-493.

[18] M.S. Patterson, B.C. Wilson, and D.R. Wyman, "The propagation of optical radiation in tissue I. Models of radiation transport and their applications," *Lasers Med. Sci.,* vol. 6, 1990, 155-166.

[19] L. Wang, S.L. Jacques, and L. Zheng, "MCML – Monte Carlo modeling of light transport in multi-layered tissues," *Computer Methods and Programs in Biomedicine,* vol. 47, 1995, pp. 131-146.

[20] F. Jaillon and H. Saint-Jalmes, "Description and time reduction of a Monte Carlo code to simulate propagation of polarized light through scattering media," *Appl. Opt.,* vol. 42, 2003, pp. 3290-3296.

[21] B. Kaplan, G. Ledanois, and B. Drevillon, "Mueller matrix of dense polystyrene latex sphere suspensions: measurements and Monte Carlo simulations," *Appl. Opt.*, vol. 40, 2001, pp. 2769-2777.

[22] M. Moscoso, J.B. Keller, and G. Papanicolaou, "Depolarization and blurring of optical images by biological tissues," *J. Opt. Soc. Am. A.,* vol.18, 2001, pp. 949-960.

[23] J.R. Mourant, T.M. Johnson, and F.P. Freyer, "Characterization of mammalian cells and cell phantoms by polarized backscattering fiber-optic measurements," *Appl. Opt.,* vol. 40, 2001, pp. 5114-5123.

[24] S. Bartel and A.H. Hielscher, "Monte Carlo simulations of the diffuse backscattering Mueller matrix for highly scattering media," *Appl. Opt.,* vol. 39, 2000, pp. 1580-1588.

[25] W. Wang and L.V. Wang, "Propagation of polarized light in birefringent media: A Monte Carlo study," *J. Biomed. Opt.,* vol. 7, 2002, pp. 350-358

[26] H.C. van de Hulst, *Light Scattering by Small Particles*, Dover, New York, 1981.

[27] M.F.G. Wood, X. Guo, and I.A. Vitkin, "Polarized light propagation in multiply scattering media exhibiting both linear birefringence and optical activity: Monte Carlo model and experimental methodology," *J. Biomed. Opt.,* vol. 12, 2007, 014029.

[28] R. Clark Jones, "New calculus for the treatment of optical systems. VII. Properties of the N-matrices," *J. Opt. Soc. Am.*, vol. 38, 1948, pp. 671-685.

[29] D.S. Kliger, J.W. Lewis, and C.E. Randall, *Polarized Light in Optics and Spectroscopy*, Academic Press–Harcourt Brace Jovanovich, New York, 1990.

[30] J. Schellman and H.P. Jenson, "Optical spectroscopy of oriented molecules," *Chem. Rev.*, vol. 87, 1987, pp. 1359-1300.

[31] S. Yau Lu and R.A. Chipman, "Interpretation of Mueller matrices based on polar decomposition", *J. Opt. Soc. Am. A*, vol. 13, 1996, pp. 1106 – 1113.

[32] J. Morio and F. Goudail, "Influence of the order of diattenuator, retarder, and polarizer in polar decomposition of Mueller matrices," *Opt. Lett.*, vol. 29, 2004, pp. 2234-2236.

[33] S. Manhas, M.K. Swami, P. Buddhiwant, N. Ghosh, P.K. Gupta and K. Singh, "Mueller matrix approach for determination of optical rotation in chiral turbid media in backscattering geometry," *Opt. Exp.*, vol. 14, 2006, pp. 190 – 202.

[34] R.A. Chipman, "*Polarimetry*," Chap. 22 in *Handbook of Optics*, 2^{nd} ed., M. Bass, Ed., Vol. 2, pp. 22.1–22.37, McGraw-Hill, New York, 1994.

[35] C. Brosseau, *Fundamentals of Polarized Light: A Statistical Optics Approach*, Wiley, New York, 1998.

[36] I.S. Sokolnikoff, *Mathematical Theory of Elasticity*, Krieger, Malabar, 1983.

[37] X. Guo, M.F.G. Wood, and I.A. Vitkin, "Monte Carlo study of pathlength distribution of polarized light in turbid media," *Opt. Exp.*, vol. 5, 2007, pp. 1348-1360.

[38] X. Guo, M.F.G. Wood, and I.A. Vitkin, "Stokes polarimetry in multiply scattering chiral media: effects of experimental geometry," *Appl. Opt.*, vol. 46, 2007, pp. 4491-4500.

[39] X. Guo, M.F.G. Wood, and I.A. Vitkin, "Detection depth and sampling volume of polarized light in turbid media," *Opt. Commun.*, 2007, SK-4383R1 (in press).

[40] K. Murayama, K. Yamada, R. Tsenkova, Y. Wang, and Y. Ozaki, "Near-infrared spectra serum albumin and γ-globulin and determination of their concentrations in phosphate buffer solution by partial least squares regression," *Vibr. Spectros.*, vol. 18, 1998, pp. 33-40.

[41] G. Yoon, A.K. Amerov, K.J. Jeon, and Y. Kim, "Determination of glucose concentration in a scattering medium on selected wavelengths by use of an overtone absorption band," *Appl. Opt.*, vol. 41, 2002, pp. 1469-1475.

[42] S. Kasemsumran, Y. Du, K. Murayama, M. Huehne, and Y. Ozaki, "Simultaneous determination of human serum albumin, γ-globulin, and glucose in a

phosphate buffer solution by near-infrared spectroscopy with moving window partial least-squares regression," *Analyst,* vol. 128, 2003, pp. 1471-1477.

[43] Y. Kim, and G. Yoon, "Prediction of glucose in whole blood near-infrared spectroscopy: influence of wavelength region, preprocessing, and hemoglobin concentration," *J. Biomed. Opt.,* vol. 11, 2006, 041128.

[44] B. Jirgensons, *Optical Rotatory Dispersion of Proteins and Other Macromolecules*, Springer-Verlag, New York, 1969.

[45] M. Otto, *Chemometrics: Statistics and Computer Application in Analytical Chemistry* 2nd ed., Wiley, New York, 2007.

[46] M.F.G. Wood, D. Côté, and I.A. Vitkin, "Combined optical intensity and polarization methodology for analyte concentration determination in simulated optically clear and turbid biological media," *J. Biomed. Opt.* (in press).